

A Parallel High-Order Accurate Finite Element Nonlinear Stokes Ice-Sheet Model and Benchmark Experiments*

Wei Leng[†] Lili Ju[‡] Max Gunzburger[§] Stephen Price[¶] Todd Ringler^{||}

Abstract

A parallel finite element implementation on tetrahedral grids of the nonlinear three-dimensional nonlinear Stokes model for the dynamics of ice-sheets is presented. Discretization is based on a high-order accurate scheme using the Taylor-Hood element pair. Both no-slip and sliding boundary conditions at the ice-bedrock boundary are studied. In addition, effective solvers using preconditioning techniques for the saddle-point system resulting from the discretization are discussed and implemented. We demonstrate through established ice-sheet benchmark experiments that our finite element nonlinear Stokes model performs at least as well as other published and established Stokes models in the field, and the parallel solver is shown to be efficient, robust, and scalable.

1 Introduction

Over the past decades, glacier and ice-sheet simulation has been a subject of growing interest because of the influential role they play in global sea-level and climate change studies [2, 5, 7, 12, 32]. Among the numerous different types of approaches employed, the three-dimensional nonlinear Stokes ice-sheet model appears to be a widely accepted method owing to its capability for dealing with realistic parameters and boundary conditions [14, 15, 19, 28, 30, 31]. Although many numerical methods such as finite difference, finite volume, and finite element have been utilized for ice-sheet modeling, the question arises as to whether they are also applicable to large scale, high-resolution simulations of realistic glaciers and ice sheets. Therefore, high-order accurate numerical approximations of the nonlinear Stokes model and parallel solvers become highly desired because the former can greatly reduce the size of the resulting discrete system while maintaining comparable solution accuracy relative to low-order methods and the latter can significantly reduce the computational costs.

Given realistic data from land and space-based observatories [1, 22–24], another key component is a high-quality, adaptive, variable resolution meshing scheme that can often significantly reduce the computational costs compared to the use of quasi-uniform grids. Numerical schemes and

*This work was partially supported by the US DOE Office of Science Climate Change Prediction Program through DE-FG02-07ER64431, DE-FG02-07ER64432, and DOE 07SCPF152, and by the US National Science Foundation under grant number DMS-0913491.

[†]State Key Laboratory of Scientific and Engineering Computing, Chinese Academy of Sciences, P.O. Box 2719, Beijing 100190, China. Email: w1eng@1sec.cc.ac.cn.

[‡]Department of Mathematics, University of South Carolina, Columbia, SC 29208, USA. Email: ju@math.sc.edu.

[§]Department of Scientific Computing, Florida State University, Tallahassee, FL 32306, USA. Email: mgunzburger@fsu.edu.

[¶]Theoretical Division, Los Alamos National Laboratory, Los Alamos, NM 87545, USA. Email: sprice@lanl.gov.

^{||}Theoretical Division, Los Alamos National Laboratory, Los Alamos, NM 87545, USA. Email: ringler@lanl.gov.

implementations on three-dimensional tetrahedral grids for ice sheet modeling are thus very welcome due to their flexibility for adaptive computation.

In this paper, we focus on the development of a parallel high-order accurate finite element solver for the nonlinear Stokes equation for large-scale ice-sheet modeling. The numerically stable Taylor-Hood element pair is used for the numerical discretization of the Stokes equation, resulting in third-order accuracy on variable resolution grids for the velocity approximation and second-order accuracy for the pressure approximation. Note that the velocity field of the ice sheet is of great interest in glacier or ice sheet studies so that our discretization approach is very attractive. In the parallel solver, Message Passing Interface (MPI) is used for data communication between the processes.

In a previous paper [34], the authors also considered three-dimensional finite element discretization of the three-dimensional nonlinear Stokes model for ice sheets. This paper differs in several important ways. First, in [34], only second-order accurate piecewise linear finite element discretizations are considered whereas now we consider third-order accurate discretizations. In addition, in [34], a penalty method is used to stabilize the finite element method employed; this introduces a nonphysical penalty parameter into the problem that not only affects accuracy, but also the conditioning of the linear systems one has to solve. The Taylor-Hood element pair used here does not need stabilization so that there is no need to introduce a penalty term for stabilization. More important, in [34], only the no-slip boundary condition at the ice-bedrock boundary is considered whereas here we consider sliding conditions as well. Thus, this paper significantly improves [34] on using higher-order accurate discretizations result in lower computational costs and handling sliding boundary conditions enables the use of the finite element ice-sheet model for realistic ice-sheet applications.

The paper is organized as follows. In Section 2, we provide a short review about the nonlinear Stokes ice-sheet model, including governing equations and boundary conditions. We also define a variational formulation of the Stokes system which is used, in Section 3, to define high-order finite element approximations, the corresponding discretized systems, and preconditioning techniques used in our solution process. Next, in Section 4, we discuss a specific process for anisotropic tetrahedral grid generation for ice sheets and the parallel implementation of the solver. In Section 5, we provide results of some validations using the established ISMIP-HOM benchmark experiments. Performance and parallel scalability of our codes are studied in Section 6. Brief concluding remarks are given in Section 7.

2 The nonlinear Stokes ice sheet model

2.1 Governing equations

The dynamical behavior of the ice sheet is modeled by the nonlinear Stokes equations for a viscous fluid in a low Reynolds-number flow over the time interval $(0, t_{max}]$ and in the three-dimensional spatial domain Ω_t occupied by the ice sheet. The system is considered incompressible so that the kinematic equation, also known as the divergence-free condition, is included as well:

$$\rho \frac{d\mathbf{u}}{dt} = \nabla \cdot \sigma + \rho \mathbf{g} \quad \text{in } \Omega_t \times (0, t_{max}] \quad (1)$$

$$\nabla \cdot \mathbf{u} = 0 \quad \text{in } \Omega_t \times (0, t_{max}], \quad (2)$$

where $\mathbf{u} = (u_1, u_2, u_3)^T$ denotes the velocity, σ is the full stress tensor, ρ is the density of ice, and $\mathbf{g} = (0, 0, -\|\mathbf{g}\|)$ denotes the gravitational acceleration, respectively. σ can be decomposed in terms

of deviatoric stress τ and the static pressure p as

$$\sigma = \tau - p\mathbf{I} \quad \text{or} \quad \sigma_{ij} = \tau_{ij} - p\delta_{ij}, \quad (3)$$

where $p = -\frac{1}{3}\text{tr}(\sigma)$, δ_{ij} denotes the Kröneckner delta tensor, and \mathbf{I} the unit tensor. Assuming that the entire material derivative $\frac{d\mathbf{u}}{dt}$ is neglected in (1) (because the time scale of variations of the velocity and pressure fields is large), we obtain the *instantaneous* momentum balance equation

$$-\nabla \cdot \tau + \nabla p = \rho\mathbf{g} \quad \text{in } \Omega_t \times (0, t_{max}]. \quad (4)$$

The strain rate tensor $\dot{\epsilon}_{\mathbf{u}}$ is then the function of displacement speed defined as

$$(\dot{\epsilon}_{\mathbf{u}})_{ij} = \frac{1}{2} \left(\frac{\partial u_i}{\partial x_j} + \frac{\partial u_j}{\partial x_i} \right). \quad (5)$$

The constitutive law for ice relates the deviatoric stress τ_{ij} to the strain rate tensor $\dot{\epsilon}_{ij}$ by the generalized Glen's flow law [25, 29]

$$\tau = 2\eta_{\mathbf{u}}\dot{\epsilon}_{\mathbf{u}} \quad (6)$$

with

$$\eta_{\mathbf{u}} = \frac{1}{2}A^{-1/n}\dot{\epsilon}_e^{(1-n)/n}, \quad (7)$$

where n is the power-law exponent, $\eta_{\mathbf{u}}$ is the temperature- and strain rate-dependent rheology coefficient (referred to as the effective viscosity), A denotes the deformation rate factor (Glen's flow law), and $\dot{\epsilon}_e$ is the effective strain rate defined as

$$\dot{\epsilon}_e = \sqrt{\frac{1}{2}\dot{\epsilon}_{\mathbf{u}} : \dot{\epsilon}_{\mathbf{u}}} = \sqrt{\frac{1}{2}((\dot{\epsilon}_{\mathbf{u}})_{11}^2 + (\dot{\epsilon}_{\mathbf{u}})_{22}^2 + (\dot{\epsilon}_{\mathbf{u}})_{33}^2 + 2(\dot{\epsilon}_{\mathbf{u}})_{12}^2 + 2(\dot{\epsilon}_{\mathbf{u}})_{23}^2 + 2(\dot{\epsilon}_{\mathbf{u}})_{31}^2)}. \quad (8)$$

If the system is assumed to be isothermal, then A is a spatially uniform constant.¹ Obviously, the constitutive relationship is a function of the strain rate. In general, it is typically assumed as a thermodynamic quasi-steady-state during the Stokes solution process.

If the top surface of the ice-sheet is allowed to evolve in time, then a prognostic equation describing the evolution of that free surface should also be included. The ice-sheet domain Ω_t at a time t can be defined as

$$\Omega_t = \{(x, y, z) \mid z_b(x, y) \leq z \leq z_s(x, y, t) \text{ for } (x, y) \in \Omega_H, t \in [0, t_{max}]\}, \quad (9)$$

where Ω_H denotes the horizontal extent of the ice sheet, $z_s(x, y, t)$ defines the top surface elevation, $z_b(x, y)$ defines the fixed bottom surface of the ice sheet. We denote the top surface as Γ_s and the bottom surface as Γ_b . In general, $z_b(x, y) \neq z_s(x, y, t)$ along the boundary of Ω_H so that the ice sheet also has a lateral boundary Γ_ℓ .

We impose a kinematic boundary resulting in the *free surface* equation:

$$\frac{\partial z_s}{\partial t} + u_1(z_s)\frac{\partial z_s}{\partial x} + u_2(z_s)\frac{\partial z_s}{\partial y} - u_3(z_s) = b(z_s, t) \quad \text{on } \Gamma_s, \quad (10)$$

where $b(z_s, t)$ represents the surface mass balance and Γ_s the top surface of the ice sheet. If the surface accumulation/ablation is zero, one usually sets $b = 0$.

¹Otherwise, A is a temperature dependent. It obeys an *Arrhenius* relation defined by

$$A = A(T) = a \exp(-Q/RT),$$

where a is an empirical flow constant often used as a tuning parameter, Q denotes the activation energy, R the universal gas constant, and T the absolute temperature measured in degrees Kelvin [34].

2.2 Boundary conditions

At the top surface of the ice sheet, we impose the boundary condition

$$\boldsymbol{\sigma} \cdot \mathbf{n} = -p_{atm} \cdot \mathbf{n} \quad \text{on } \Gamma_s, \quad (11)$$

where \mathbf{n} denotes the outer normal vector of the ice sheet boundary and p_{atm} the atmospheric pressure. Along the lateral boundary Γ_ℓ we impose one of three types of boundary conditions; a condition such as (11), a no-slip condition $\mathbf{u} = 0$, or periodic boundary conditions. The bottom surface of the ice sheet can be decomposed into two parts, $\Gamma_{b,fix}$ and $\Gamma_{b,sld}$, where $\Gamma_{b,fix}$ denotes the part that is fixed to the bottom bedrock and $\Gamma_{b,sld}$ the part that is allowed to slide. Thus, we obtain the following conditions:

$$\mathbf{u} = 0 \quad \text{on } \Gamma_{b,fix} \quad (12)$$

which is referred to as the *no-slip* boundary condition and

$$\mathbf{u} \cdot \mathbf{n} = 0 \quad \text{and} \quad \mathbf{n} \cdot \boldsymbol{\sigma} \cdot \mathbf{t} = -\beta^2 \mathbf{u} \cdot \mathbf{t} \quad \text{on } \Gamma_{b,sld} \quad (13)$$

which is referred to as the *Rayleigh friction* boundary condition. The parameter β^2 denotes a given sliding coefficient and \mathbf{t} denotes any unit vector tangential to the bottom surface. Note that the negative sign in (13) implies that the direction of the friction force is opposite to that of the velocity.

2.3 Variational formulation

Finite element discretizations are based on variational formulations of the partial differential equation system; in this section we derive a variational formulation of the Stokes system (1)-(2).

Let $L^2(\Omega_t)$ denote the space of square-integrable functions with respect to Ω_t and let $\mathbf{H}^1(\Omega_t) = (H^1(\Omega_t))^3$, where $H^1(\Omega_t)$ denotes the subspace of $L^2(\Omega_t)$ consisting of functions whose first derivatives also belong to $L^2(\Omega_t)$. Multiply (1) by a test function $\mathbf{v} \in \mathbf{H}_1(\Omega_t)$, then integrate the result over Ω_t , and the integrating by parts results in

$$\int_{\Omega_t} \boldsymbol{\tau} : \nabla \mathbf{v} \, d\mathbf{x} - \int_{\Omega_t} p \nabla \cdot \mathbf{v} \, d\mathbf{x} - \int_{\Gamma} \mathbf{n} \cdot \boldsymbol{\sigma} \cdot \mathbf{v} \, ds = \rho \int_{\Omega_t} \mathbf{g} \cdot \mathbf{v} \, d\mathbf{x}, \quad (14)$$

where $\Gamma = \Gamma_s \cup \Gamma_b \cup \Gamma_\ell$ and $\boldsymbol{\tau} : \nabla \mathbf{v}$ denotes the sum of the element-wise products of the tensors $\boldsymbol{\tau}$ and $\nabla \mathbf{v}$. Note that, because $\nabla \cdot \mathbf{u} = 0$, we obtain

$$\int_{\Omega_t} \boldsymbol{\tau} : \nabla \mathbf{v} \, d\mathbf{x} = \int_{\Omega_t} 2\eta_{\mathbf{u}} \dot{\boldsymbol{\epsilon}}_{\mathbf{u}} : \dot{\boldsymbol{\epsilon}}_{\mathbf{v}} \, d\mathbf{x}. \quad (15)$$

Note that $\mathbf{n} \cdot \boldsymbol{\sigma} = -p_{atm} \mathbf{n}$ on Γ_s so that

$$\int_{\Gamma_s} \mathbf{n} \cdot \boldsymbol{\sigma} \cdot \mathbf{v} \, ds = \int_{\Gamma_s} -p_{atm} \mathbf{n} \cdot \mathbf{v} \, ds. \quad (16)$$

Here we simply set $p_{atm} = 0$. With this simplification, we also have

$$\int_{\Gamma_\ell} \mathbf{n} \cdot \boldsymbol{\sigma} \cdot \mathbf{v} \, dx = 0, \quad (17)$$

where, depending on what type of boundary condition we impose along the lateral boundary Γ_ℓ , we also require the test function \mathbf{v} to satisfy $\mathbf{v}|_{\Gamma_\ell} = 0$ (for the no-slip boundary condition) or \mathbf{v}

periodic (for the periodic boundary condition). If we further restrict \mathbf{v} such as $\mathbf{v}|_{\Gamma_{b,fix}} = 0$, then we also have

$$\int_{\Gamma_{b,fix}} \mathbf{n} \cdot \boldsymbol{\sigma} \cdot \mathbf{v} \, ds = 0. \quad (18)$$

On the bottom sliding boundary $\Gamma_{b,slid}$, because $\mathbf{u} \cdot \mathbf{n} = 0$, we can naturally require the test function to satisfy $\mathbf{v} \cdot \mathbf{n} = 0$. Together with the friction law $\mathbf{n} \cdot \boldsymbol{\sigma} \cdot \mathbf{t} = -\beta^2 \mathbf{u} \cdot \mathbf{t}$, we then have that

$$-\int_{\Gamma_{b,slid}} \mathbf{n} \cdot \boldsymbol{\sigma} \cdot \mathbf{v} \, ds = \int_{\Gamma_{b,slid}} \beta^2 \mathbf{u} \cdot \mathbf{v} \, ds. \quad (19)$$

Let

$$\tilde{\mathbf{H}}(\Omega_t) = \{\mathbf{u} \in \mathbf{H}^1(\Omega_t) \mid \mathbf{u}|_{\Gamma_t \cup \Gamma_{b,fix}} = 0, (\mathbf{u} \cdot \mathbf{n})|_{\Gamma_{b,slid}} = 0\}.$$

Note that functions in $\tilde{\mathbf{H}}(\Omega_t)$ satisfy homogeneous boundary conditions on the indicated parts of the boundary.

Substituting (15)-(19) into (14), we obtain the weak formulation of the nonlinear Stokes model (1)-(2): seek $\mathbf{u} \in \tilde{\mathbf{H}}(\Omega_t)$ and $p \in L^2(\Omega_t)$ such that

$$\begin{cases} \int_{\Omega_t} 2\eta_{\mathbf{u}} \dot{\boldsymbol{\varepsilon}}_{\mathbf{u}} : \dot{\boldsymbol{\varepsilon}}_{\mathbf{v}} \, d\mathbf{x} + \int_{\Gamma_{b,slid}} \beta^2 \mathbf{u} \cdot \mathbf{v} \, ds - \int_{\Omega_t} p \nabla \cdot \mathbf{v} \, d\mathbf{x} = \rho \int_{\Omega_t} \mathbf{g} \cdot \mathbf{v} \, d\mathbf{x} \\ - \int_{\Omega_t} q \nabla \cdot \mathbf{u} \, d\mathbf{x} = 0 \end{cases} \quad (20)$$

for all $\mathbf{v} \in \tilde{\mathbf{H}}(\Omega_t)$ and $q \in L^2(\Omega_t)$. If the free surface equation (10) is used to evolve the ice sheet, then its weak form is to find $z_s \in H^1(\Omega_H)$, such that

$$\int_{\Gamma_s} \frac{\partial z_s}{\partial t} \psi \, ds = \int_{\Gamma_s} \left(u_3 - u_1 \frac{\partial z_s}{\partial x} - u_2 \frac{\partial z_s}{\partial y} + b \right) \psi \, ds, \quad \text{for all } \psi \in H^1(\Omega_H). \quad (21)$$

In practical simulations, we have to divide the time interval $[0, t_{max}]$ into K subintervals $\{[t_{k-1}, t_k]\}_{k=1}^K$, where $t_k = k\Delta t$ and $\Delta t = t_{max}/K$. Then, a semi-discrete (in time) variational problem using the forward Euler scheme is to seek z_s^{k+1} on Γ_{s,t_k} such that

$$\int_{\Gamma_{s,t_k}} z_s^{k+1} \psi \, ds = \int_{\Gamma_{s,t_k}} z_s^k \psi \, ds + \int_{\Gamma_{s,t_k}} \Delta t \left(u_3^k - u_1^k \frac{\partial z_s^k}{\partial x} - u_2^k \frac{\partial z_s^k}{\partial y} + b^k \right) \psi \, ds, \quad (22)$$

$$k = 0, 1, \dots, K-1,$$

where z_s^k denotes the top surface height at time t_k , b^k the surface accumulation/ablation at t_k , Γ_{s,t_k} the top surface of the ice sheet at t_k , and z_s^0 is given as an initial condition.

3 High-order accurate finite element approximation

3.1 Discretized system by finite elements

Let \mathcal{T}_h be a tetrahedral triangulation of the ice domain Ω_t . Here, h is a measure of the spatial grid size, e.g., the maximum diameter of any of the tetrahedral elements. Now, we spatially discretize the variational form of the Stokes equation (20). The finite element space $P_{1,h}(\mathcal{T}_h)$ used for approximating the pressure consists of functions that, within each tetrahedral element, is a linear polynomial, e.g., in x, y, z space, they are functions of the form $a_0 + a_1x + a_2y + a_3z$ for constants a_i , $i = 0, \dots, 3$. Such functions are uniquely determined by their values at the four

vertices of a tetrahedral element. For approximation of the components of velocity, we instead use a higher-order finite element space, $P_{2,h}(\mathcal{T}_h)$ that consists of quadratic polynomials inside each of the tetrahedra, e.g., in x, y, z space, they are functions of the form $b_0 + b_1x + b_2y + b_3z + b_4x^2 + b_5y^2 + b_6z^2 + b_7xy + b_8yz + b_9zx$ for constants b_i , $i = 0, \dots, 9$. These functions can be uniquely determined by their values at the four vertices and the six midsides of the edges of a tetrahedron. See Figure 1 for an illustration. In addition, the functions in both $P_{1,h}$ and $P_{2,h}$ are required to be continuous across element faces. This pair of elements for discretizing the Stokes equation is referred to as the Taylor-Hood element pair and satisfies the LBB stability condition (or inf-sup condition) [13] required for stable approximations. We then define the constrained space (in case the lateral boundary condition is a no-slip boundary condition)

$$\tilde{\mathbf{P}}_{2,h}(\mathcal{T}_h) = \{\mathbf{u}_h \in (P_{2,h}(\mathcal{T}_h))^3 \mid \mathbf{u}_h|_{\Gamma_l \cup \Gamma_{b,fix}} = 0, (\mathbf{u}_h \cdot \mathbf{n})|_{\Gamma_{b,std}} = 0\}. \quad (23)$$

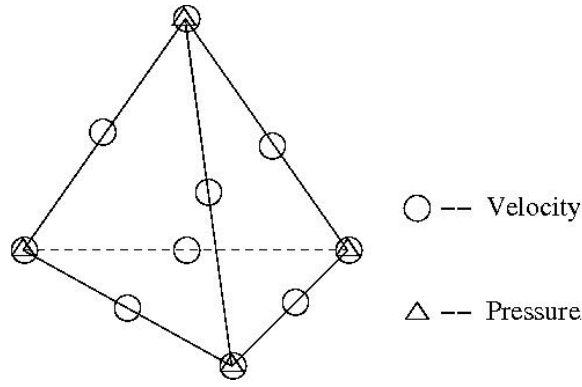


Figure 1: The Taylor-Hood (P2-P1) element.

Thus, given Ω_t and \mathcal{T}_h , we seek functions $\mathbf{u}_h \in \tilde{\mathbf{P}}_{2,h}(\mathcal{T}_h)$ and $p_h \in P_{1,h}(\mathcal{T}_h)$ such that

$$\begin{cases} \int_{\Omega_t} 2\eta_{\mathbf{u}_h} \varepsilon_{\mathbf{u}_h} : \varepsilon_{\mathbf{v}_h} d\mathbf{x} + \int_{\Gamma_{b,std}} \beta^2 \mathbf{u}_h \cdot \mathbf{v}_h ds - \int_{\Omega_t} p_h \nabla \cdot \mathbf{v}_h d\mathbf{x} = \rho \int_{\Omega_t} \mathbf{g} \cdot \mathbf{v}_h d\mathbf{x} \\ - \int_{\Omega_t} q_h \nabla \cdot \mathbf{u}_h d\mathbf{x} = 0 \end{cases} \quad (24)$$

for all $\mathbf{v}_h \in \tilde{\mathbf{P}}_{2,h}(\mathcal{T}_h)$ and $q_h \in P_{1,h}(\mathcal{T}_h)$.

We use a direct Picard-type iterative algorithm to solve the nonlinear system (24), i.e., the variables used for evaluation of the velocity-dependent viscosity $\eta_{\mathbf{u}}$ for the j -th step are taken from the $(j-1)$ -th iteration step of the algorithm as follows:

$$\begin{cases} \int_{\Omega_t} 2\eta_{\mathbf{u}_h^{(j-1)}} \varepsilon_{\mathbf{u}_h^{(j)}} : \varepsilon_{\mathbf{v}_h} d\mathbf{x} + \int_{\Gamma_{b,std}} \beta^2 \mathbf{u}_h^{(j)} \cdot \mathbf{v}_h ds - \int_{\Omega_t} p_h^{(j)} \nabla \cdot \mathbf{v}_h d\mathbf{x} = \rho \int_{\Omega_t} \mathbf{g} \cdot \mathbf{v}_h d\mathbf{x} \\ - \int_{\Omega_t} q_h \nabla \cdot \mathbf{u}_h^{(j)} d\mathbf{x} = 0 \end{cases} \quad (25)$$

and, finally, set $\mathbf{u}_h = \mathbf{u}_h^{(j)}$ when satisfactory convergence is achieved. The finite element approximation (25) produces, at each iteration, a symmetric saddle point problem of the type

$$\begin{pmatrix} F & B^T \\ B & \mathbf{0} \end{pmatrix} \begin{pmatrix} \tilde{\mathbf{u}} \\ \tilde{p} \end{pmatrix} = \begin{pmatrix} \tilde{\mathbf{r}} \\ 0 \end{pmatrix}. \quad (26)$$

Thus, we only need an efficient linear system solver. We expect that this nonlinear solver is linearly convergent with a contraction constant $\frac{n-1}{n}$, where n denotes the exponent in the Glen's flow law. It is known that the error of such approximation is of third-order accuracy in the velocity \mathbf{u} (i.e., $O(h^3)$) and of second order accuracy in the pressure p (i.e., $O(h^2)$) [3].

For the approximation of the top surface $z_s(x, y, t)$ during evolution, we use the linear finite element space $P_{1,h}(\mathcal{Q}_h)$ consisting of continuous piecewise linear polynomials defined with respect to the two-dimensional triangular triangulation \mathcal{Q}_h of the horizontal extent of the ice sheet, i.e., of Ω_H . Note that we assume that Ω_H is fixed. Then, the fully discretized (in time and space) free-surface equation can be described as follows: for $k = 0, 1, \dots, K-1$, given $\mathbf{u}_{h,k}$, we solve $z_{s,h} \in P_{1,h}(\mathcal{Q}_h)$

$$\int_{\Gamma_{s,t_k}} z_{s,h}^{k+1} \psi_h ds = \int_{\Gamma_{s,t_k}} z_{s,h}^k \psi_h ds + \int_{\Gamma_{s,t_k}} \Delta t \left(v_3^k - v_1^k \frac{\partial z_{s,h}^k}{\partial x} - v_2^k \frac{\partial z_{s,h}^k}{\partial y} + b^k \right) \psi_h ds \quad (27)$$

for all $\psi_h \in P_{1,h}(\mathcal{Q}_h)$. Once \mathbf{u}^k has been determined, we can easily update the elevation of the top surface $z_{s,h}^{k+1}$ and thus determine the new domain $\Omega_{t_{k+1}}$. Note that at each time step, after the computation of surface elevation, the grid points should be redistributed according to the surface movement to avoid distortion.

3.2 Implementation of the sliding boundary constraints

A remaining important problem is how to handle the sliding boundary conditions. Let us assume the degree of freedom (DOF) in velocity is $3M$, where M is the number of grid points for velocity, and rewrite the velocity vector $\tilde{\mathbf{u}}$ in (26) in the form of

$$\tilde{\mathbf{u}} = \begin{pmatrix} \mathbf{u}_1 \\ \vdots \\ \mathbf{u}_M \end{pmatrix}$$

with $\mathbf{u}_i = (u_{i,1}, u_{i,2}, u_{i,3})^T$. Constraints need to be imposed on $\Gamma_{b,sld}$ such that

$$\mathbf{n}_i \cdot \mathbf{u}_i = 0, \quad \text{for all } i \in \sigma_{b,sld}, \quad (28)$$

where $\sigma_{b,sld}$ denotes the set of indices of the DOF of \mathbf{u} that lie on the sliding boundary $\Gamma_{b,sld}$ and \mathbf{n}_i denotes the outer normal of the surface corresponding to the i -th DOF.

For each DOF $i \in \sigma_{b,sld}$ on the sliding boundary, a local coordinate system is built with one surface normal vector \mathbf{n}_i and two orthonormal surface tangential vectors \mathbf{t}_i^1 and \mathbf{t}_i^2 . Define the 3×3 transformation matrix

$$T_i = (\mathbf{n}_i, \mathbf{t}_i^1, \mathbf{t}_i^2).$$

As for the DOF that do not lie on the sliding boundary, define the corresponding transformation matrix to be the 3×3 identity matrix I , i.e., $T_i = I$ if $i \notin \sigma_{b,sld}$. Then, we obtain a global transformation matrix for all i ,

$$T = \begin{pmatrix} T_1 & & \\ & \ddots & \\ & & T_m \end{pmatrix}.$$

Note that $T^T T = I$. Inserting T into the linear system (26), we have

$$\begin{pmatrix} \tilde{F} & \tilde{B}^T \\ \tilde{B} & \mathbf{0} \end{pmatrix} \begin{pmatrix} \tilde{\mathbf{u}} \\ \tilde{p} \end{pmatrix} = \begin{pmatrix} \tilde{\mathbf{r}} \\ \mathbf{0} \end{pmatrix} \quad (29)$$

where

$$\tilde{F} = TFFT^T, \quad \tilde{B} = BT^T, \quad \tilde{\mathbf{u}} = T\mathbf{u}, \quad \tilde{\mathbf{r}} = T\mathbf{r}.$$

Now let us take $\tilde{\mathbf{u}}$ as unknowns. Note that

$$(\tilde{\mathbf{u}})_i = (\mathbf{n}_i \cdot \mathbf{u}_i, \mathbf{t}_i^1 \cdot \mathbf{u}_i, \mathbf{t}_i^2 \cdot \mathbf{u}_i)^T = (0, \mathbf{t}_i^1 \cdot \mathbf{u}_i, \mathbf{t}_i^2 \cdot \mathbf{u}_i)^T \quad \forall i \in \sigma_{b,sld}.$$

Thus, we can simply apply zero Dirichlet boundary condition on the first component of each $(\tilde{\mathbf{u}})_i$. After solving (29) for $\tilde{\mathbf{u}}$, we simply set $\mathbf{u} = T^T(\tilde{\mathbf{u}})$.

3.3 Linear solvers and preconditioning

The linear system (29) is a saddle point problem and is often very ill-conditioned, thus a preconditioning process is needed. Considering the block factorization of the coefficient matrix

$$\begin{pmatrix} \tilde{F} & \tilde{B}^T \\ \tilde{B} & \mathbf{0} \end{pmatrix} = \begin{pmatrix} \mathbf{I} & \mathbf{0} \\ \tilde{B}\tilde{F}^{-1} & \mathbf{I} \end{pmatrix} \begin{pmatrix} \tilde{F} & \tilde{B}^T \\ \mathbf{0} & -S \end{pmatrix}, \quad (30)$$

where $S = \tilde{B}\tilde{F}^{-1}\tilde{B}^T$ is the Schur complement. We use the upper triangular factor

$$M^{-1} = \begin{pmatrix} \tilde{F}^{-1} & \tilde{B}^T \\ \mathbf{0} & -S^{-1} \end{pmatrix} \quad (31)$$

as the right preconditioner. Because the Schur complement S involves solving \tilde{F}^{-1} , we replace it by a weighted mass matrix $\hat{S} := M_\mu$, where $(M_\mu)_{i,j} = \int_{\Omega_t} \mu^{-1} \phi_i \phi_j dx_1 dx_2 dx_3$ and ϕ_i denotes a pressure basis function. For varying viscosity, the resulting matrix is spectrally equivalent to the Schur complement [26, 27]. This preconditioner is very effective when the sub-problem \tilde{F}^{-1} is solved exactly, but of course we can only solve \tilde{F}^{-1} iteratively, and in that case, the preconditioner is highly sensitive to the residual of the \tilde{F}^{-1} solve. We will regard the \tilde{F}^{-1} solve as the inner iteration and the GMRES solve as the outer iteration for the solution of (30).

A solver for the sub-problem \tilde{F}^{-1} should at least handle the following three obstacles properly:

1. *anisotropy* – the computing grid could have very thin shaped elements, e.g., with aspect ratio up to 100;
2. *highly variable viscosity* – the viscosity across the computing domain could differ by factor of 1000;
3. *symmetric gradient* – the equation uses the symmetric gradient $\nabla \mathbf{u} + \nabla \mathbf{u}^T$ so that the sub-problem is a linear elasticity problem and not a Poisson problem.

The Algebraic Multigrid (AMG) method [4] solver is a reasonable choice for the \tilde{F}^{-1} because it can handle highly variable coefficients and anisotropy nicely; further, it is a very efficient solver for linear elasticity problem if a proper strategy is used. Geometric multigrid methods probably also could play a role here because techniques such as semi-coarsening and line smoothing are quite effective for anisotropic problems. However, in the case of ice-sheet modeling, the highly variable viscosity is the main difficulty that has to be overcome by using operator-dependent interpolation and Galerkin coarse grid operator, and these techniques all fall into the AMG category.

Parallel AMG solver *BoomerAMG* from the *hypre* package [9] was used in our parallel implementation. *BoomerAMG* has a great flexibility to choose between various parallel coarsening strategies and different interpolation operators. The setting of AMG greatly affects the efficiency of the solver; choices of AMG settings for different problems are studied in Section 6.

4 Grid generation and parallel implementation

Due to the high aspect ratio of the ice sheet which results in a high aspect ratio grid, some special treatment during the generation of the tetrahedral grids is needed to avoid bad-quality elements. Our approach is to first generate a high-quality, two-dimensional triangular grid for the horizontal extent of the ice sheet Ω_H . The two-dimensional grid is then transformed to a three-dimensional surface triangular grid for the top surface of the ice sheet by adding the z -coordinate obtained from the topography of the bedrock plus the ice thickness. We then produce a fully three-dimensional prismatic mesh of the ice sheet domain Ω_t by mapping the surface meshes linearly along the z -direction down to the bedrock. Finally, we obtain a tetrahedral grid of the ice sheet by decomposing each of the prismatic elements into three tetrahedra.

During the surface evolution, after the computation of top surface elevation z_s , the grid points should be redistributed according to the surface movement to avoid distortion. Linear or nonlinear elasticity analogs could be used to deform the mesh. However, for simplicity, a linear mapping is applied to determine the z -coordinates of the mesh vertexes. The governing equation reads,

$$\begin{aligned} \frac{\partial Z}{\partial z} &= 1 && \text{on } \Omega_t \\ Z &= z_s && \text{on } \Gamma_s \\ Z &= z_b && \text{on } \Gamma_b, \end{aligned} \tag{32}$$

where Z denotes the z -coordinate of the mesh vertexes. If the initial mesh is uniform in the z direction at each horizontal grid point, this linear mapping ensures that subsequent meshes are likewise uniform in the z direction.

Parallel computations often apply a *divide and conquer* strategy to solve large-scale problems. In our parallel solvers, we used the preconditioned GMRES method for solution of the linear system and adopted the *domain decomposition method* (DDM) [10, 33] for construction of the coefficient matrix and the local preconditioning on distributed computer processors. The finite element meshes are first partitioned into a number of sub-meshes whose number is consistent with the number of processors to be used in the parallel calculation. This results in dividing the computing domain Ω_{t_k} at the time step t_k into interconnected sub-domains. By doing so, the original large-scale computing problem is decomposed into a group of relatively simpler and smaller problems on different processors. Our grid partitioning is done only in the horizontal direction using "METIS", a family of multilevel mesh partitioning algorithms [17]; see Figure 2 for an illustration.

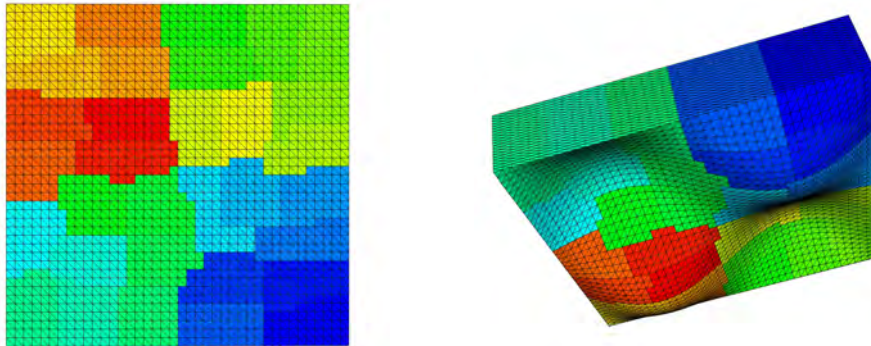


Figure 2: Partition of a sample tetrahedral grid into 32 subgrids. Left: two-dimensional view from the top; right: three-dimensional view.

The large, sparse linear systems arising from the finite element discretization may have millions of unknowns in order to obtain high-resolution in the numerical simulations. Solving such large-scale systems is a challenging task due to the high demand on computing power and memory. Iterative solution techniques for massive linear systems based on Krylov subspace methods (such as GMRES and conjugate gradient methods) as well as preconditioning techniques (such as block, multi-grid, and incomplete LU factorization preconditioners [18]) are commonly used because the Krylov subspace iteration methods require only matrix-vector products. Message Passing Interface (MPI) is taken as the parallel environment. We use the GMRES method together with the block and Algebraic Multi-Grid (AMG) preconditioning techniques for the solution of (29) in our implementation; in particular, the popular software package PETSC (<http://www.mcs.anl.gov/petsc/>) is employed in our parallel implementation due to its reliability and robustness. Some detailed discussions are given in Section 6. We also would like to note that, for the above horizontal partitioning, parallel coarsening using AMG will have fewer difficulties in handling the inter-processor boundary and data communication.

5 ISMIP-HOM benchmark tests

We tested our parallel, high-order accurate FEM nonlinear Stokes ice-sheet model using the ISMIP-HOM Benchmark problems [30]. There are six experiments (Experiments A-F) in this Benchmark suite [30]. For all experiments, because the horizontal extent of the ice sheet Ω_H is a rectangle, we used tetrahedral grids produced from a uniform two-dimensional structured triangular meshes so that periodic boundary conditions in the lateral boundaries can be easily applied. We use the parameters given in [30] for the ice sheet; see Table 1.

Name	Symbol	Value	Units
Deformation rate factor	A	10^{-16} (Exp. A-E) 2.140373×10^{-17} (Exp. F)	$Pa^{-n} a^{-1}$
Power law exponent	n	3 (Exp. A-E) 1 (Exp. F)	—
Ice density	ρ	910	$kg\ m^{-3}$

Table 1: Parameters and constants for ISMIP-HOM benchmark experiments for the nonlinear Stokes ice sheet modeling.

5.1 Experiments A and B: ice flow with no-slip basal boundary condition

Experiment A considers ice flow over a bumpy bed in an idealized geometry, i.e., we have a parallel-sided slab of ice having a mean thickness of $1000\ m$ lying on a sloping bed with a mean slope $\alpha = 0.5^\circ$. The basal topography of the ice sheet is then defined as a series of sinusoidal oscillations with an amplitude of $500\ m$:

$$z_b(x, y) = z_s(x, y) - 1000 + 500 \sin(\omega x) \sin(\omega y) \quad (33)$$

with the top surface is given by

$$z_s(x, y) = -x \tan(\alpha). \quad (34)$$

Here, $(x, y) \in [0, L] \times [0, L]$. Note that the basal bumps have a frequency of $\omega = 2\pi/L$. The no-slip boundary condition $\mathbf{u} = \mathbf{0}$ is imposed at the bottom boundary of the ice sheet (thus $\Gamma_{b,slid} = \emptyset$). On the lateral boundaries, periodic boundary conditions are imposed.

The set-up for Experiment B is the same except that the basal topography does not vary in y , i.e., we have

$$z_b(x, y) = z_s(x, y) - 1000 + 500 \sin(\omega x) \quad (35)$$

so that in this case we have ice flow over a rippled bed.

The ice-sheet length L is set to increase by a factor of two in each successive experiment, starting $L = 5 \text{ km}$ and ending $L = 160 \text{ km}$.² Our numerical simulation results for the surface velocity components at different length scales for Experiments A and B are shown in Figures 3 and 4, respectively; 16 processors and a grid of 192,000 tetrahedra resulting from a $40 \times 40 \times 20$ structured prismatic mesh was used. An obvious improvement of the high-order numerical scheme vs. the low order ones even can be visually seen in the velocity component u_2 in Figure 4 (Experiment B). Although u_2 in this experiment is very small compared with u_1 and u_3 as expected, a clear pattern of u_2 is shown in our high order accurate simulations while not in the results of [34] which used a low-order linear finite element approximations.

Our results match very well with the results of [11] which also used a Stokes finite element simulation but with a finer $60 \times 60 \times 30$ mesh for Experiment A and $240 \times 120 \times 30$ for Experiment B. The norm of surface velocity across the bump at $y = L/4$ is shown and compared with the reference solution from [11] in Figures 5 and 6.

5.2 Experiments C and D: ice-stream flow and basal sliding condition

Experiments C and D consider the case of ice-stream flow and basal sliding conditions. The geometry setup of the ice sheet in Experiment C is similar to Experiment A except that $\alpha = 0.1^\circ$ and the basal topography is flat, i.e.,

$$z_b(x, y) = z_s(x, y) - 1000. \quad (36)$$

Periodic boundary conditions are still imposed on the lateral boundaries, but on the bottom surface a basal friction boundary condition is imposed everywhere (thus $\Gamma_{b,fix} = \emptyset$) with

$$\beta^2(x, y) = 1000 + 1000 \sin(\omega x) \sin(\omega y). \quad (37)$$

The setup of Experiment D is the same as Experiment C except that the basal friction coefficient is set to

$$\beta^2(x, y) = 1000 + 1000 \sin(\omega x). \quad (38)$$

Simulation results for the surface velocity components at different length scales for Experiments C and D are shown in Figures 7 and 8, respectively, using the same grid (except the elevation in the z direction) as that used for Experiments A and B. The norm of surface velocity across the bump at $y = L/4$ is shown and compared with the reference solution in Figures 9 and 10. Again, our results match the results in [11].

5.3 Experiment E: Haut Glacier d’Arolla

Experiment E is a diagnostic experiment along the central flowline of a temperate glacier in the European Alps (Haut Glacier d’Arolla). The basic experiment and geometry is described in [6]. Input for the model is formed by the longitudinal surface and bedrock profiles of Haut Glacier d’Arolla, Switzerland. The longitudinal profile of this glacier has a very simple geometry; see Figure 11.

²As we move towards the shorter wavelengths, it successively pushes the “higher-order” parts of the model harder and harder (i.e., they contribute relative more to the stress balance), whereas at the longest wavelength, the solution for the model is essential the same as that for an SIA model [30].

We run Experiment E for two different basal boundary conditions: (I) without sliding zone, i.e., the no-slip condition $\mathbf{u} = 0$ (or say $\beta^2 = +\infty$) is imposed on the basal boundary; (II) with a sliding zone defined by

$$\beta^2 = \begin{cases} 0 & \text{if } 2200m \leq x \leq 2500m \\ +\infty & \text{otherwise.} \end{cases} \quad (39)$$

For both cases, zero velocity conditions are imposed on the lateral boundary in the x direction and periodic boundary conditions are imposed in the y direction.

Two different grids are generated using the dataset of the Haut Glacier d’Arolla longitudinal profile, which has 51 points of location, bedrock elevation and surface elevation. The first grid, denoted by E_1_10, uses only one interval between the dataset points of the geometry from the profile, whereas the second grid uses 10 intervals, denoted by E_10_10, and both grids have 10 layers in vertical direction. The mesh vertex coordinates between dataset points were generated using linear interpolation. Although linear interpolation would result in oscillation of the solution, it defines an unique region to carry out the experiments; besides, it could represent the situation in which there is indeed some discontinuities in geometry. For other applications, as suggested in [11], smoother interpolation such as Nonuniform Rational B-Splines (NURBS), could be chosen.

Simulation results of Arolla flow without sliding zone are shown in Figures 12 (left) and 13. The surface velocities for both grids are quite smooth and show good agreement with the reference solution, but the basal shear stresses and the pressure differences show certain oscillations and roughly match the reference solution, especially for the coarse grid case. One interval between two dataset points is not enough; higher resolution is clearly needed to capture all the features. The solution on the fine grid E_10_10 is smooth between two dataset points, however, near the dataset points sudden changes still appear. We can conclude that the solution, especially to high order accurate models such as the model proposed here, is quite sensitive to the geometry; rough boundary descriptions such as linear interpolation on the boundary could lead to solutions with small oscillations.

The results of Arolla flow with a sliding zone are shown in Figures 12 (right) and 14. Because this experiment includes a sliding zone, a singularity could appear near the singular points where friction parameter β^2 suddenly change from zero to infinity. The results using the coarse grid E_1_10 are inaccurate; as we can see, the velocity is relatively smaller and the peak of the basal stress and pressure difference is smoothed out. The results using the fine grid E_10_10 show agreement with the reference solution for the surface velocity. Strong singularities of the basal stress and the pressure difference appear near the singular points; we believe that adaptively locally refined grids or isoparametric elements can be used to resolve this issue.

5.4 Experiment F: a prognostic example

Experiment F is a prognostic example for which the top surface is allowed to evolve in time according to equation (10) until a steady state is reached, i.e., zero surface mass balance holds such that

$$\lim_{t \rightarrow +\infty} \frac{\partial z_s}{\partial t} = 0. \quad (40)$$

A slab of ice with mean ice thickness $H^{(0)} = 1000m$ is considered, lying on a sloping bed with a mean slope $\alpha = 3.0^\circ$. This slope is maximum in x and zero in y . The initial top surface elevation is

$$z_s^{(0)}(x, y) = -x \tan \alpha \quad (41)$$

and the bedrock plane z_b is parallel to the initial top surface plane and is perturbed by a Gaussian bump such that

$$z_b(x, y) = -H^{(0)} - x \tan \alpha + \gamma_0 e^{-(x^2+y^2)/\sigma^2} \quad (42)$$

with $\gamma = 0.1H^{(0)}$ and $\sigma = 10H^{(0)}$. The horizontal domain of the ice sheet is taken to be a square $[-L/2, L/2] \times [-L/2, L/2]$ with size $L = 100H^{(0)}$. It is also assumed that there is no surface accumulation/ablation. Periodic boundary conditions are applied in the horizontal directions and a sliding boundary condition is imposed on the bottom with

$$\beta^2 = (cAH^{(0)})^{-1}. \quad (43)$$

We test two cases for Experiment F: (I) non-slippery case, i.e., $c = 0$, and (II) slippery case with $c = 1$. Note that in this experiment, because $n = 1$, the effective viscosity is constant and is given by $\eta_{\mathbf{u}} \equiv (2A)^{-1}$ so that the Picard iteration is not needed.

The time dependent model is run using our parallel implementation, again on the same tetrahedral grid (except for the elevation in the z direction) as for Experiments A and B with a time step of 5 years. We also note the z -coordinates of the grid points are recalculated at each time step to maintain the mesh quality as mentioned in Section 4. In our test, a steady state is assumed to be reached if the change of the top surface elevation between two time steps is small enough, e.g., less than $10^{-2}m$. From our simulation, the time it takes for the thickness of the ice sheet to be stabilized in the non-slippery case and slippery case are about 375 and 1245 years, respectively. The steady state results and convergence history are shown in Figures 15, 16, and 17. Our results show good agreement with the two reference solutions in [11] and [20].

6 Performance and scalability

Our parallel high-order FEM solver worked very well with all experiments. The stopping criterion for the GMRES method is set to 1.0e-9 and that for the Picard iteration to 1.0e-4. We first present tests of the performance of the preconditioned GMRES linear system solver. A grid of 192,000 tetrahedra was produced from a starting structured prismatic mesh with a $40 \times 40 \times 20$ decomposition of the domain; the number of DOF for the discretized system is 827,604. For different experiments, three different AMG parameter settings were used, as listed in Table 2; the first setting was also used by Burstedde in [8, 21]. Because the AMG solver serves in the inner iteration, the most time consuming part of AMG in our test is the cycling. Settings of the AMG solver and numbers for inner iterations used in our experiments are listed in Table 3, and numbers for the outer GMRES iterations are listed in Table 4.

Parameter Setting No.	a	b	c
Coarsening	PMIS	PMIS	Falgout
Interpolation	extended	extended	classical
Truncation factor	0.3	0.3	0.
Strong threshold	0.5	0.9	0.5
Max entries per row for interp	5	5	0
Number of Functions	3	3	1
Coarsest Relax Type	direct	direct	direct

Table 2: The BoomerAMG parameter settings used in our parallel solver.

Length Scale	Exp. A	Exp. B	Exp. C	Exp. D
$L = 5km$	a,1	a,1	c,3	c,3
$L = 10km$	a,1	a,1	c,3	c,6
$L = 20km$	a,1	a,1	c,3	c,6
$L = 40km$	a,1	b,1	c,3	c,6
$L = 80km$	a,1	b,1	c,3	c,6
$L = 160km$	a,1	b,1	c,3	c,6

Table 3: The AMG settings and cycle numbers of the sub-problems in Experiments A-D.

From the table it is easy to see that our linear solver worked very well for all experiments, i.e., it used only a few number of outer GMRES iterations. Another fact we learn from Table 4 is that problems with sliding boundary are more difficult than the ones with a no-slip boundary, requiring roughly 3 to 6 times number of inner iterations to effect similar reductions in the residual of the problem. This is usually due to the worse condition of the linear system resulted from the sliding boundary conditions.

Length Scale	Exp. A	Exp. B	Exp. C	Exp. D
$L = 5km$	19	28	31	56
$L = 10km$	17	27	32	26
$L = 20km$	16	30	25	25
$L = 40km$	17	31	29	34
$L = 80km$	24	33	41	30
$L = 160km$	24	30	38	50

Table 4: Numbers of the outer GMRES iterations of the preconditioned solver in Experiments A-D.

In parallel computing, two types of scalability are commonly used to measure the performance. The first one is the strong scalability S_{strong} which reflects how the solution time varies with the number of processors for a fixed total problem size. The second is the weak scalability S_{weak} which shows how the solution time varies with the number of processors for a fixed problem size per processor. Since we used four processors as the smallest number of processors in all tests, then we calculated S_{strong} and S_{weak} as

$$S_{strong} = \frac{4 * T_4}{n * T_n}, \quad S_{weak} = \frac{T_4}{T_n}$$

where T_n denotes the solution time with n processors. A value greater than 1.0 implies super-linear scaling.

The first test is for weak scalability, i.e., we test our solver with proportionally increasing number of processors but a fixed subproblem size per processor. Up to 1024 processors are used to test our solver and the results are reported in Table 5. In this table, "NOIs-nonlinear" denotes the number of Picard iterations and "NOIs-linear" the number of GMRES iterations used for solving the linear system at each Picard iteration. From the table we can see that the number of iterations the linear solver used for different problem sizes is almost constant, and the total running times grow very slow as the number of processors increases until the last case with 1024 processors. This clearly shows both our preconditioning algorithm and parallel implementation have very nice weak scalability.

The second test is for strong scalability, i.e., we test our solver with increasing number of processors for a fixed total problem size. We fixed the structured mesh using the $80 \times 80 \times 20$

Mesh Size	Number of Tetrahedra	DOF	Number of Procs	NOIs -linear	NOIs -nonlinear	Total Time(s)	Scalability S_{weak}
$20 \times 20 \times 20$	48,000	208,644	4	31	25	494	-
$40 \times 40 \times 20$	192,000	827,604	16	26	25	466	1.060
$80 \times 80 \times 20$	768,000	3,296,724	64	20	25	435	1.136
$160 \times 160 \times 20$	3,072,000	13,159,764	256	19	25	525	0.941
$320 \times 320 \times 20$	12,288,000	52,585,044	1024	20	25	886	0.558

Table 5: Results of the weak scalability tests using our parallel FEM solver for Experiment A.

decomposition of the domain; the number of DOF is 3,296,724. Results are reported in Table 6. For all the tests with different number of processors, the number of interior linear iterations is 20 and the number of outer non-linear iterations is 25. From the table it is easy to see that, for number of processors no more than 32, the total time cost decreases more than half as the number of processors doubles, implying super linear scaling. For the rest of the case, the time cost decrease is not so large, and it's still endurable. This shows that our parallel solver has excellent strong scalability.

Number of Processors	Memory Usage per Core(MB)	Avg. Time(s) per Iteration	Total Time(s)	Scalability S_{strong}
4	4859	233	8090	-
8	2495	75	3030	1.335
16	1368	39	1547	1.307
32	766	22	853	1.186
64	480	12	459	1.102
128	335	8.2	288	0.878
256	267	6.6	226	0.559

Table 6: Results of the strong scalability tests using our parallel FEM solver for Experiment A. Mesh size: $80 \times 80 \times 20$, number of tetrahedral elements: 768,000, number of DOF: 3,296,724.

7 Concluding remarks

In this paper we develop a parallel finite element ice-sheet computational model for the nonlinear Stokes system in three dimensions. Our finite element model features higher-order computational accuracy compared to existing ice-sheet models and scalable parallel solvers. Moreover, it accounts for realistic basal sliding conditions along the ice-bedrock boundary. Future efforts are devoted to implementing the three-dimensional nonlinear Stokes finite element model on variable resolution grids and in particular, for Greenland and Antarctica ice-sheet modeling. Note that our tetrahedral meshing strategy based on prismatic grids is directly applicable to grids constructed using variable resolution in the horizontal directions and layers in the vertical direction. Future efforts also involve the incorporation of the ice-ocean interface into the model in addition to the ice-atmosphere and ice-bedrock interfaces treated here. Finally, future efforts also consider several implementation improvements for our ice-sheet model, including studying the impact of using NURBS refined elements in Experiments E and F to produce higher accuracy and smoother solutions and also to the design of better preconditioning for problems with sliding boundary conditions to produce more efficient solvers.

References

- [1] BAMBER, J., EKHOLM, S., AND KRABILL, W. (2001). A new, high resolution digital elevation model of Greenland fully validated with airborne laser altimeter data, *J. Geophys. Res.*, **106** (B4), pp. 6733-6745.
- [2] BENGTSSON, L. (1994). Climate of the 21st-Century, *Agricultural and Forest Meteorology*, **72**(1-2), pp. 3-29.
- [3] BERCOVIER, M., PIRONNEAU, O. (1979). Error estimates for finite element method solution of the Stokes problem in the primitive variables. *Numer. Math.*, **33**, pp. 211-224.
- [4] BRIGGS, W.L., HENSON, V.E., AND MCCORMICK, S.F. (2000). *A Multigrid Tutorial*, 2nd Edition, SIAM.
- [5] BLATTER, H. (1995). Velocity and stress fields in grounded glaciers: a simple algorithm for including deviatoric stress gradients, *J. Glaciol.*, **41**, pp. 33-44.
- [6] BLATTER, H., CLARKE, G., AND COLINGE, J. (1998). Stress and velocity fields in glaciers: Part II. sliding and basal stress distribution., *J. Glaciol.*, bf 44, pp. 457-466.
- [7] BROMWICH, D.H., BAI, L.H., AND BJARNASON, G.G. (2005). High-resolution regional climate simulations over Iceland using Polar MM5, *Monthly Weather Review*, **133**(12), pp. 3527-3547.
- [8] BURSTEDDE, C., GHATTAS O., STADLER, G., TU, T., AND WILCOX, L.C. (2009). Parallel scalable adjoint-based adaptive solution of variable-viscosity Stokes flow problems, *Comput. Methods Appl. Mech. Engrg.*, **198**, pp. 1691-1700.
- [9] FALGOUT, R.D., AND YANG, U.M. (2002). hypre: A Library of High Performance Preconditioners, Proceedings of the International Conference on Computational Science-Part III, **2331**, pp.632-641.
- [10] DOUGLAS, C.C. (1996). Multigrid methods in science and engineering, *IEEE Computational Science & Engineering*, **3**(4), pp. 55-68.
- [11] GAGLIARDINI, O., AND ZWINGER, T. (2008). The ISMIP-HOM benchmark experiments performed using the finite element code Elmer, *The Cryosphere*, **2**, pp. 67-76, doi:10.5194/tc-2-67-2008.
- [12] GREGORY, J.M., AND HUYBRECHTS, P. (2006). Ice-sheet contributions to future sea-level change, *Philosophical Transactions of the Royal Society-Mathematical, Physical and Engineering Sciences*, **364**, pp. 1709-1731.
- [13] GUNZBURGER, M. (1989). *Finite Element Methods for the Navier-Stokes Equations*, Academic, Boston.
- [14] HOLLAND, D.M., INGRAM, R.G., MYSAK, L.A., AND OBERHUBER, J.M. (1995). A numerical simulation of the sea-ice cover in the Northern Greenland sea, *Journal of Geophysical Research-Oceans*, **100**(C3), pp. 4751-4760.
- [15] HOLLAND, D.M., MYSAK, L.A., MANAK, D.K., AND OBERHUBER, J.M. (1993). Sensitivity study of a dynamic thermodynamic sea ice model, *Journal of Geophysical Research-Oceans*, **98**(C2), pp. 2561-2586.

- [16] JU, L. (2007). Conforming centroidal Voronoi Delaunay triangulation for quality mesh generation, *International Journal of Numerical Analysis and Modeling*, **4**, pp. 531-547.
- [17] KARYPIS, G. (2003). Multi-constraint mesh partitioning for contact/impact computations, *Supercomputing'03*, Phoenix, Arizona, USA.
- [18] LI, X.Y., AND DEMMEL, J.W. (2003). SuperLU_DIST: A scalable distributed-memory sparse direct solver for unsymmetric linear systems, *ACM Transactions on Mathematical Software*, **29**(2), pp. 110-140.
- [19] LE MEUR, E., GAGLIARDINI, O., ZWINGER, T., AND RUOKOLAINEN, J. (2004). Glacier flow modelling: A comparison of the shallow ice approximation and the full-Stokes solution. *Comptes Rendus Physique*, **5**(7), pp. 709-722.
- [20] MARTIN, C., NAVARRO, F., OTERO, J., CUADRADO, M., AND CORCUERA, M. (2003). Three-dimensional modelling of the dynamics of Johnson Glacier (Livingstone Island, Antarctica), *Ann. Glaciol.*, **39**, pp. 1-8.
- [21] May, D.A. and Moresi L. (2008). Preconditioned iterative methods for Stokes flow problems arising in computational geodynamics, *Phys. Earth Planet. Interiors*, **171** (1-4), pp. 33-47, DOI:10.1016/j.pepi.2008.07.036.
- [22] MERNILD, S.H., LISTON, G.E., HIEMSTRA, C.A., AND STEFFEN, K. (2008). Surface melt area and water balance modeling on the Greenland ice sheet 1995-2005, *Journal of Hydrometeorology*, **9**(6), pp. 1191-1211.
- [23] MERNILD, S.H., LISTON, G.G., KANE, D.L., KNUDSEN, N.F., AND HASHOLT, B. (2008). Snow, runoff, and mass balance modeling for the entire Mittivakkat Glacier (1998-2006), Ammassalik Island, SE Greenland, *Geografisk Tidsskrift-Danish Journal of Geography*, **108**(1), pp. 121-136.
- [24] NICK, F.M., VIELI, A., HOWAT, I.M., AND JOUGHIN, I. (2009). Large-scale changes in Greenland outlet glacier dynamics triggered at the terminus, *Nature Geoscience*, **2**(2), pp. 110-114.
- [25] NYE, J. (1957). The distribution of stress and velocity in glaciers and ice sheets, *Proc. R. Soc. London*, Ser. A, **239**, pp. 113-133.
- [26] OLSHANSKII, M.A., AND REUSKEN A. (2006). Analysis of a Stokes interface problem, *Numerische Mathematik*, **103**(1), pp. 129-149.
- [27] OLSHANSKII, M.A., PETERS, J., AND REUSKEN, A. (2006). Uniform preconditioners for a parameter dependent saddle point problem with application to generalized Stokes interface equations *Numerische Mathematik*, **105**(1), pp. 159-191.
- [28] PATTYN, F. (2003). A new 3D higher-order thermomechanical ice-sheet model: Basic sensitivity, ice-stream development and ice flow across subglacial lakes, *J. Geophys. Res.*, **108**(B8), 2382, doi:10.1029/2002JB002329, 2003.
- [29] PATERSON, W. (1994). *The Physics of Glaciers*, Elsevier Science, Oxford, U. K.

- [30] PATTYN, F., PERICHON, L., ASCHWANDEN, A., BREUER, B., SMEDT, D.B., GAGLIARDINI, O., GUDMUNDSSON, G.H., HINDMARSH, R.C.A., HUBBARD, A., JOHNSON, J.V., KLEINER, T., KONOVALOV, Y., MARTIN, C., PAYNE, A.J., POLLARD, D., PRICE, S., RUCKAMP, M., SAITO, F., SUGIYAMA, S., AND ZWINGER, T. (2008). Benchmark experiments for higher-order and full-Stokes ice sheet models (ISMIP-HOM), *The Cryosphere*, **2**, pp. 95-108.
- [31] PRICE, S.F., WADDINGTON, E.D., AND CONWAY, H. (2007). A full-stress, thermomechanical flow band model using the finite volume method, *Journal of Geophysical Research-Earth Surface*, **112**, F03020, doi:10.1029/2006JF000724.
- [32] SAITO, F. (2002). *Development of a Three Dimensional Ice Sheet Model for Numerical Studies of Antarctic and Greenland Ice Sheets*, Ph.D. thesis, Univ. of Tokyo, Tokyo, Japan.
- [33] VALLI, A.Q. (1999). *Domain Decomposition Methods for Partial Differential Equations*, Oxford Science Publications.
- [34] ZHANG, H., JU, L., GUNZBURGER, M., RINGLER, T. AND PRICE S. (2011). Coupled models and parallel simulations for three dimensional full-Stokes ice sheet modeling, *Numerical Mathematics: Theory, Methods and Applications*, to appear.

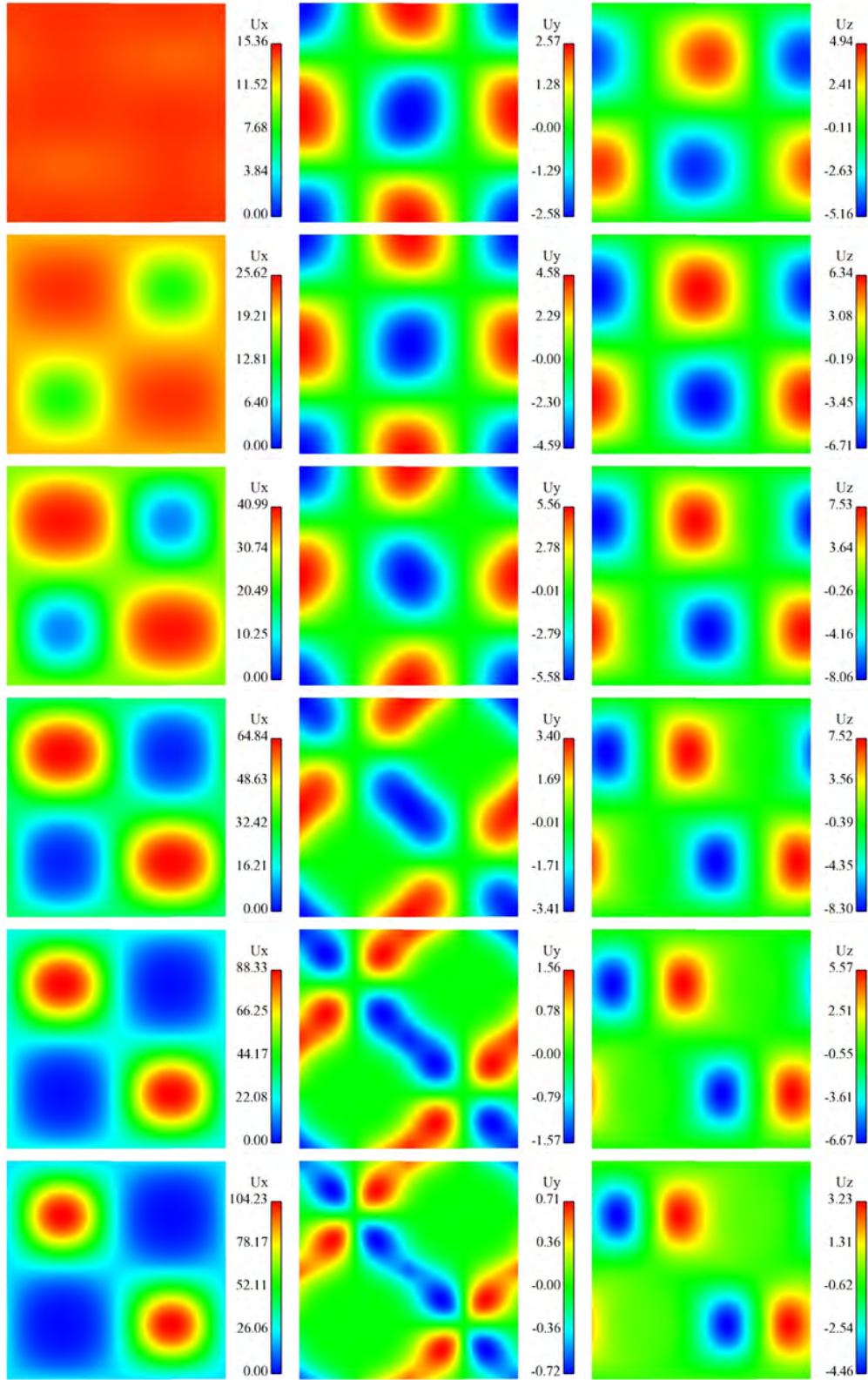


Figure 3: Simulation results at different length scales for Experiment A. From left to right: the components u_1 , u_2 , and u_3 of the top surface velocity (ma^{-1}); from top to bottom: $L = 5, 10, 20, 40, 80, 160$ km.

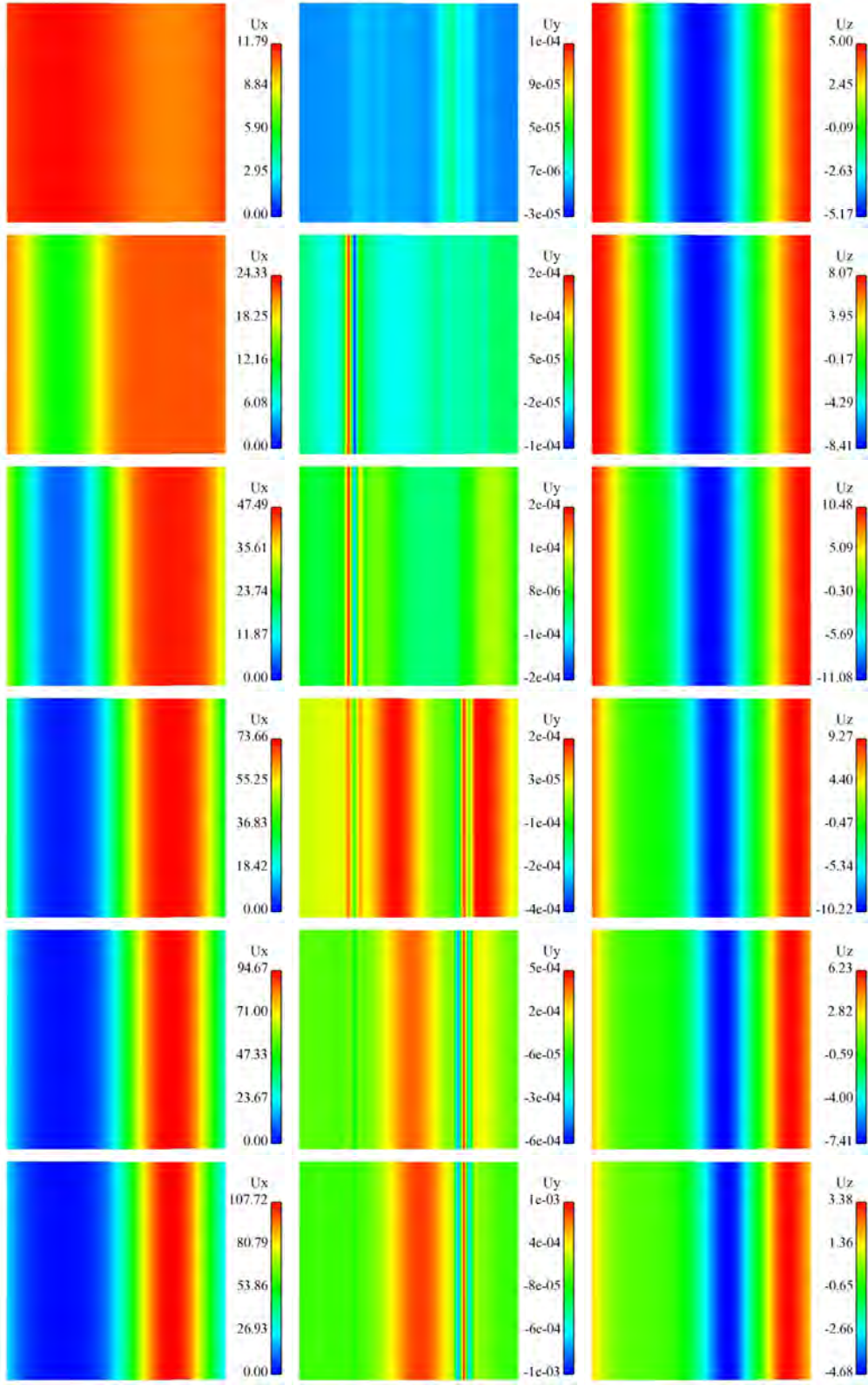


Figure 4: Simulation results at different length scales for Experiment B. From left to right: the components u_1 , u_2 , and u_3 of the top surface velocity (ma^{-1}); from top to bottom: $L = 5, 10, 20, 40, 80, 160$ km.

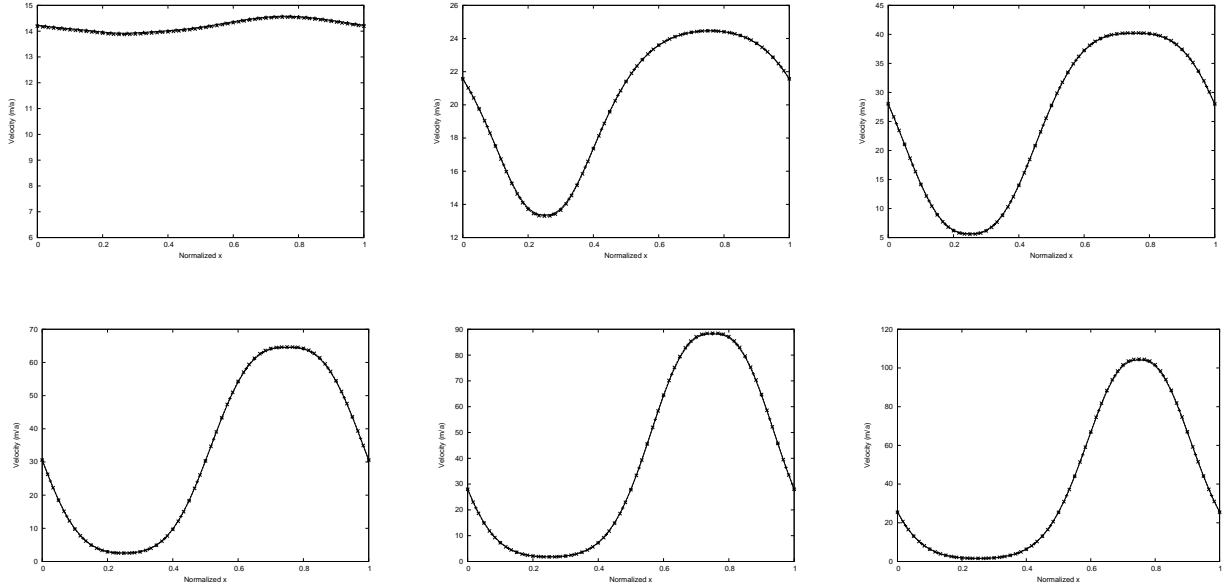


Figure 5: Norm of the surface velocity across the bump at $y = L/4$ in Experiment A at different length scales (solid lines with tick marks: our solution; dashed curve with crosses: the reference solution [11]). From left to right and from top to bottom: $L = 5, 10, 20, 40, 80, 160 \text{ km}$.

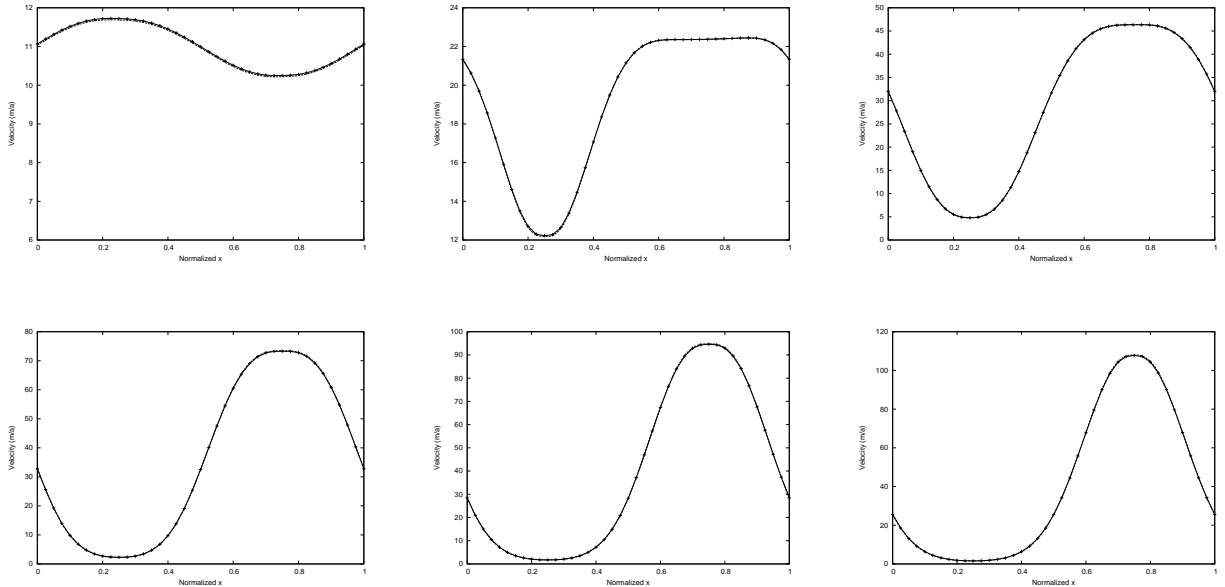


Figure 6: Norm of the surface velocity across the bump at $y = L/4$ in Experiment B at different length scales (solid lines with tick marks: our solution; dashed curve: the reference solution [11]). From left to right and from top to bottom: $L = 5, 10, 20, 40, 80, 160 \text{ km}$.

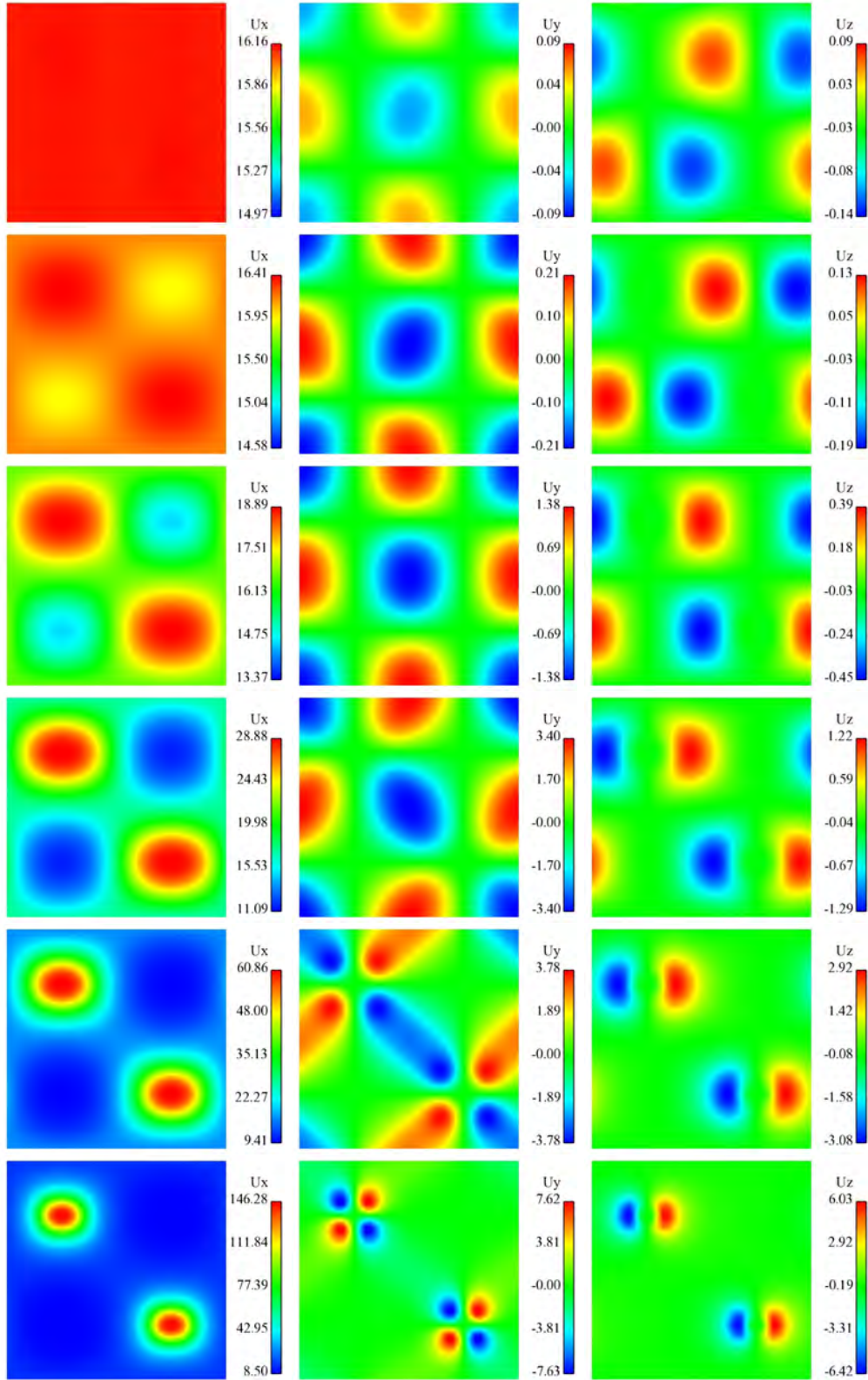


Figure 7: Simulation results at different length scales for Experiment C. From left to right: the components u_1 , u_2 , and u_3 of the top surface velocity (ma^{-1}); from top to bottom: $L = 5, 10, 20, 40, 80, 160 km$.

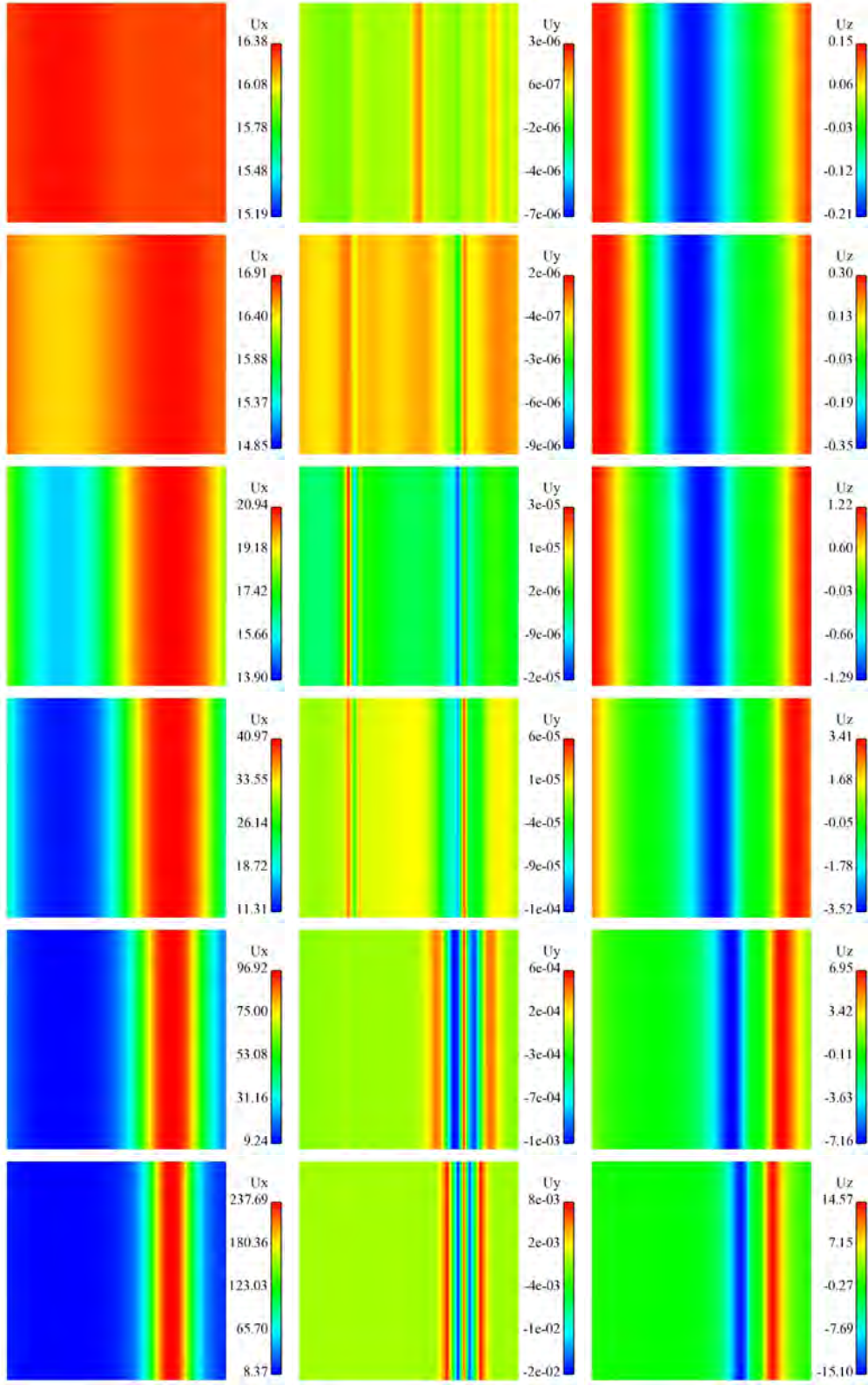


Figure 8: Simulation results at different length scales for Experiment D. From left to right: the components u_1 , u_2 , and u_3 of the top surface velocity (ma^{-1}); from top to bottom: $L = 5, 10, 20, 40, 80, 160 \text{ km}$.

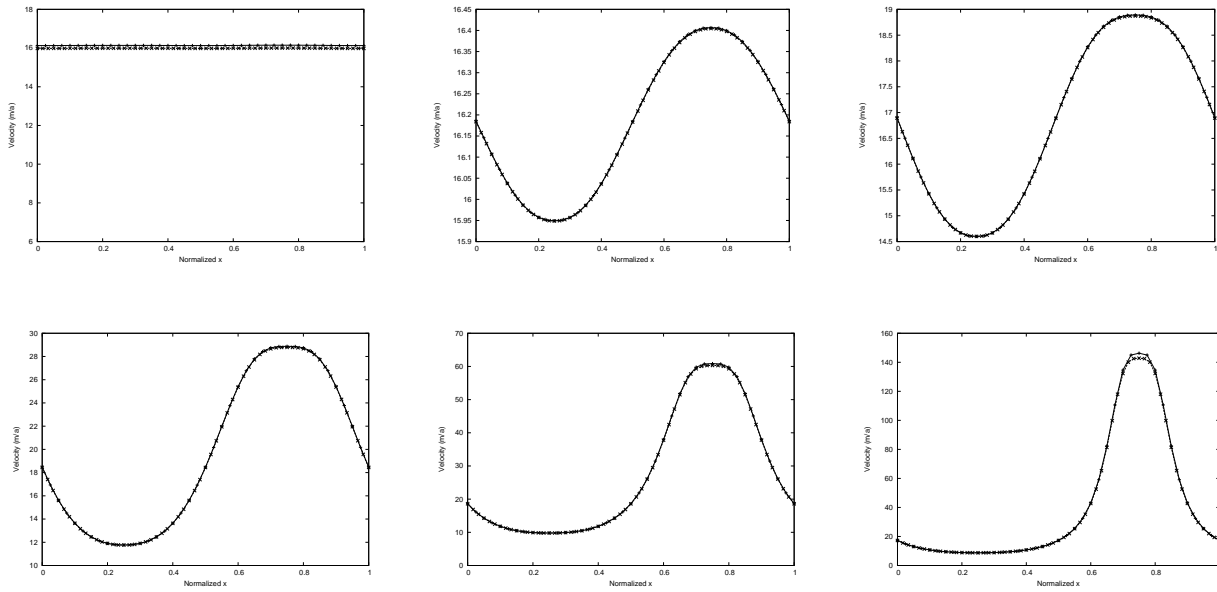


Figure 9: Norm of the surface velocity across the bump at $y = L/4$ in Experiment C at different length scales (solid lines with tick marks: our solution; dashed curve with crosses: the reference solution [11]). From left to right and from top to bottom: $L = 5, 10, 20, 40, 80, 160 \text{ km}$.

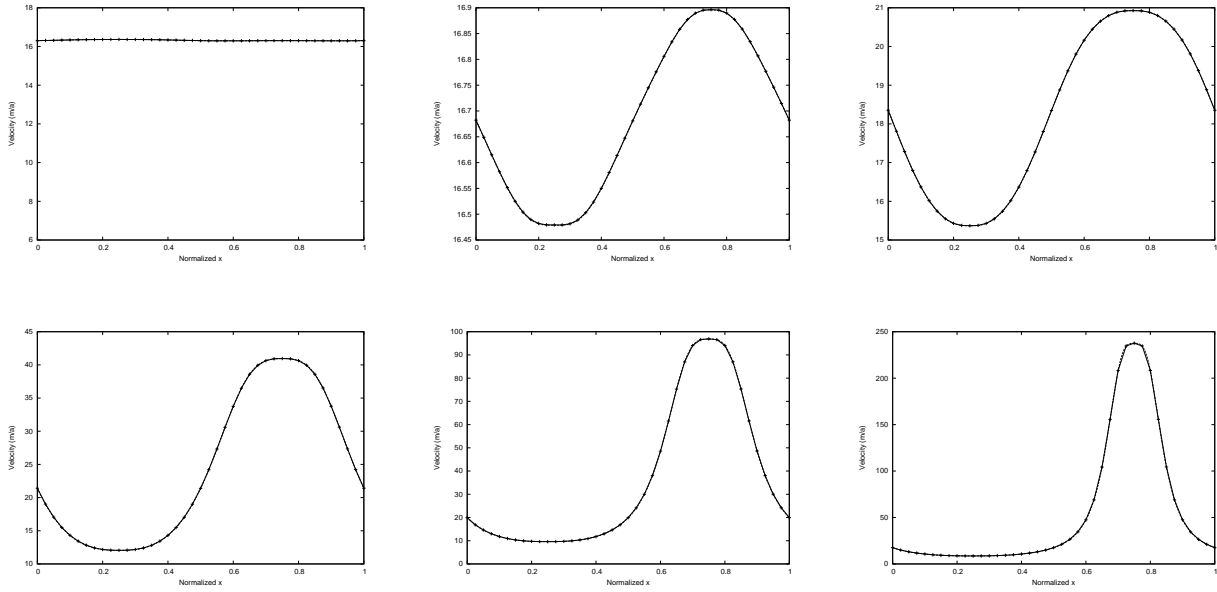


Figure 10: Norm of the surface velocity across the bump at $y = L/4$ in Experiment D at different length scales (solid lines with tick marks: our solution; dashed curve with crosses: the reference solution [11]). From left to right and from top to bottom: $L = 5, 10, 20, 40, 80, 160 \text{ km}$.

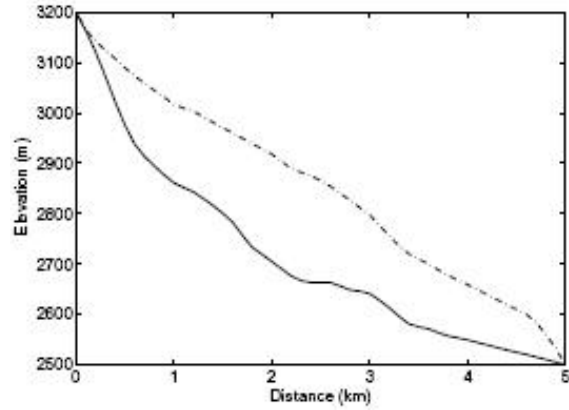


Figure 11: Surface and bedrock profiles of the Haut Glacier d'Arolla [30] in Experiment E.

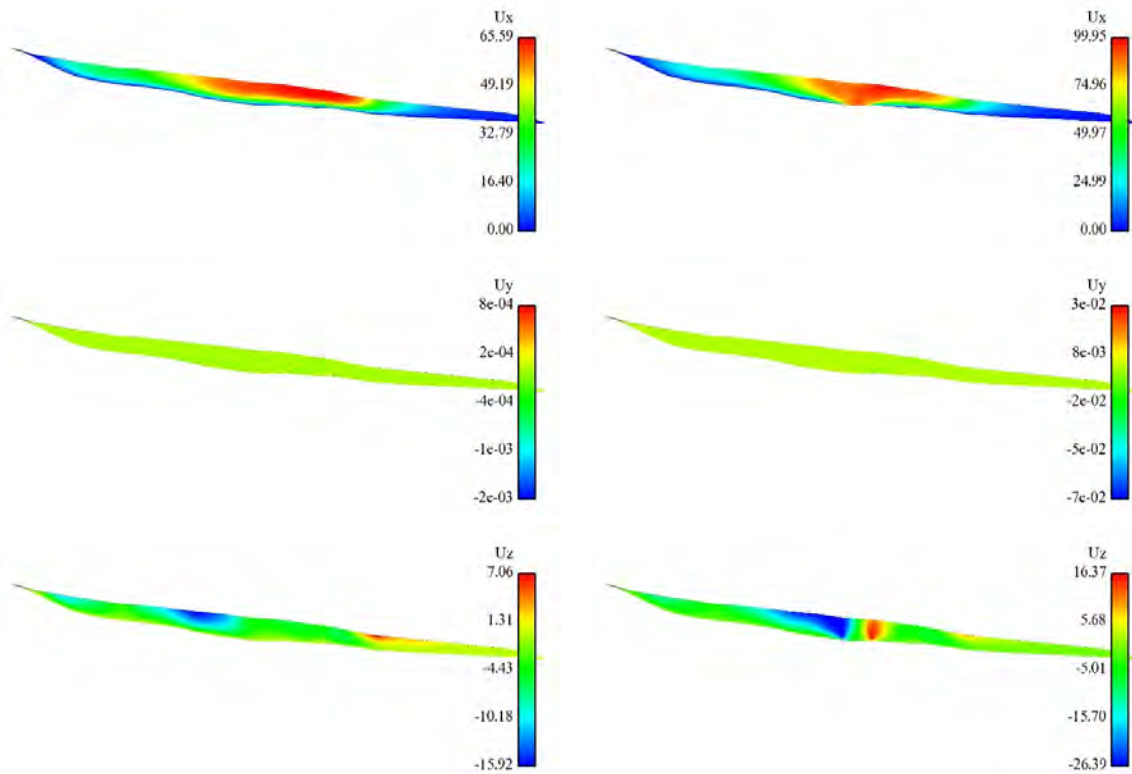


Figure 12: Simulation results (view of the middle section along the y -direction) for Experiment E. Left: Case I – without sliding zone; right: Case II – with sliding zone. From top to bottom: the components u_1 , u_2 , u_3 of the velocity.

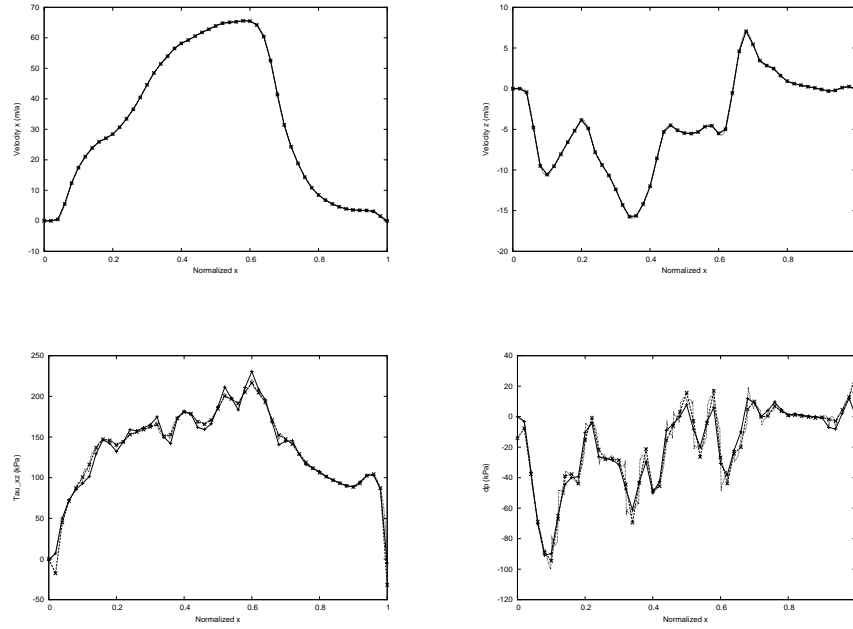


Figure 13: Simulation results for Experiment E without a sliding zone (Case I). Top to bottom and then left to right: horizontal top surface velocity (ma^{-1}); vertical top surface velocity (ma^{-1}); basal shear stress; difference between the isotropic and hydrostatic pressure at the bed. Dotted curve: fine mesh; dashed curve with crosses: coarse grid; solid curve with tick marks: the reference solution [11].

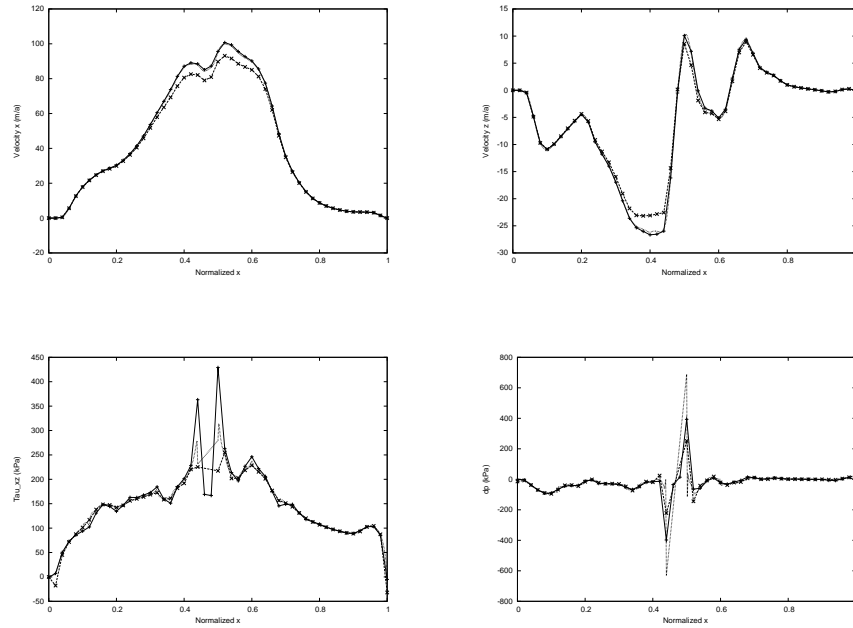


Figure 14: Simulation results of Experiment E with a sliding zone (Case II). Top to bottom and then left to right: horizontal top surface velocity (ma^{-1}); vertical top surface velocity (ma^{-1}); basal shear stress; difference between the isotropic and hydrostatic pressure at the bed. Dotted curve: fine mesh; dashed curve with crosses: coarse grid; solid curve with tick marks: the reference solution [11].

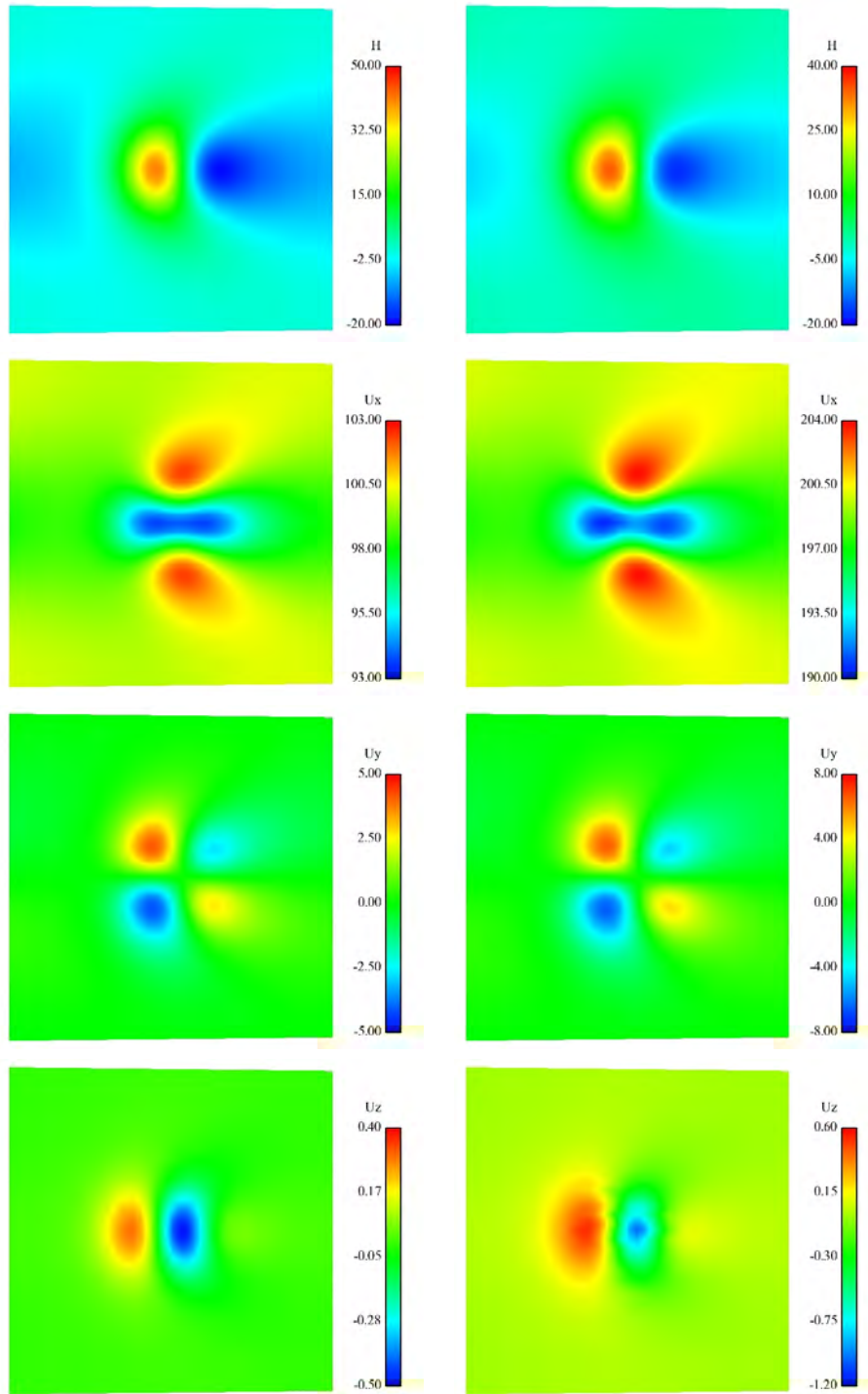


Figure 15: Simulation results for the steady state in Experiment F viewed from above the top surface. Left: Case I – non-slippery case; right: Case II – slippery case. From top to bottom: surface elevation and velocity components u_1 , u_2 , and u_3 .

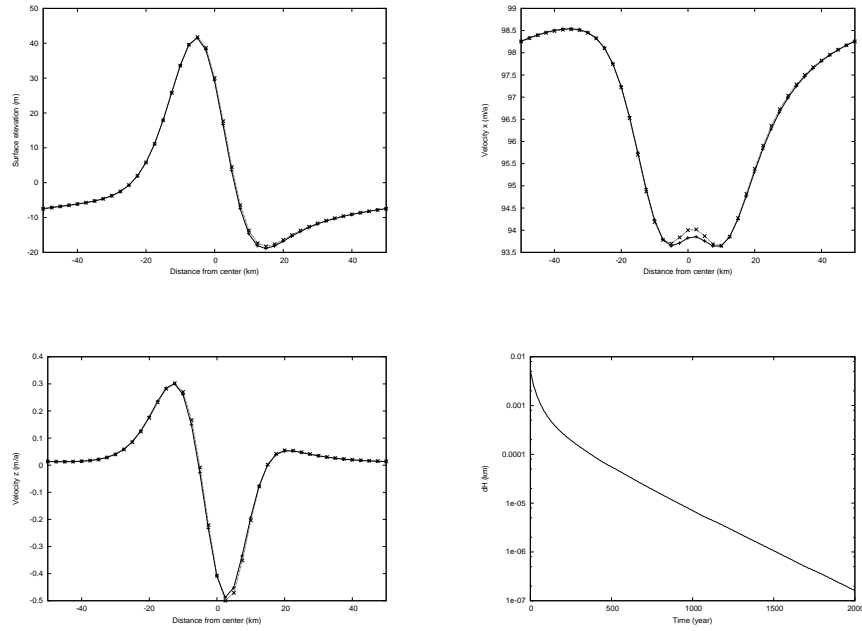


Figure 16: Simulation results for the steady state in Experiment F – Case I (non-slippery case) viewed along the central line. Top to bottom and then left to right: top surface elevation; surface velocity component u_1 ; surface velocity component u_3 ; maximum change of the surface elevation in time. Dotted curve with crosses: our solution; dashed curve with crosses: the reference solution [20].

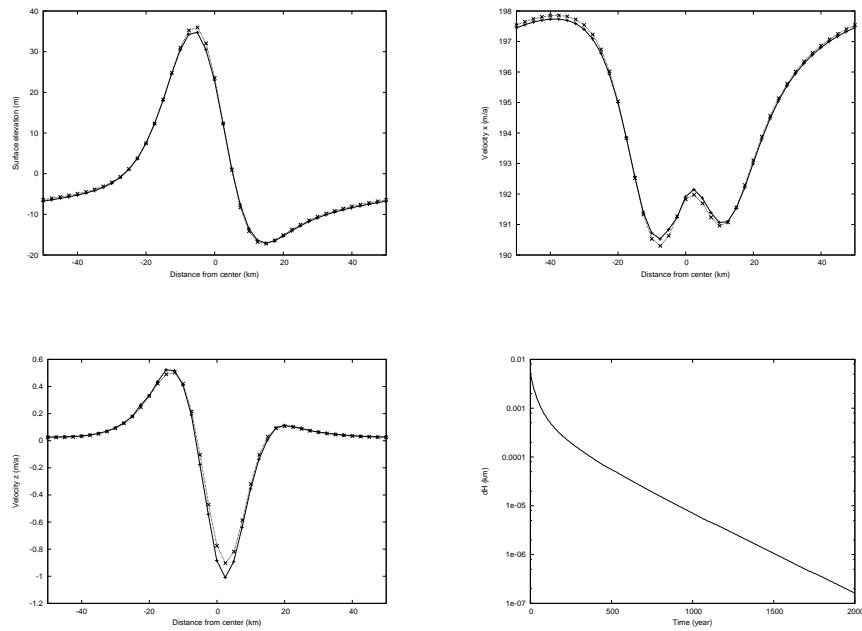


Figure 17: Simulation results of the steady state in Experiment F – Case II (slippery case) viewed along the central line. Top to bottom and then left to right: top surface elevation; surface velocity component u_1 ; surface velocity component u_3 ; maximum change of the surface elevation in time. Dotted curve with crosses: our solution; dashed curve with crosses: the reference solution [20].